A table-top monochromator for tunable femtosecond XUV pulses generated in a semi-infinite gas cell: Experiment and simulations

Author(s):
von Conta, Aaron; Huppert, Martin; Wörner, Hans Jakob

Publication date:
2016-07

Permanent link:
https://doi.org/10.3929/ethz-a-010890606

Originally published in:
Review of Scientific Instruments 87(7), https://doi.org/10.1063/1.4955263

Funding acknowledgement:
307270 - Measuring attosecond electron dynamics in molecules (EC)

A table-top monochromator for tunable femtosecond XUV pulses generated in a semi-infinite gas cell: Experiment and simulations

A. von Conta, M. Huppert and H. J. Wörner[1]
Laboratorium für Physikalische Chemie, ETH Zürich, Vladimir-Prelog-Weg 2, CH-8093 Zürich, Switzerland

(Dated: 23 May 2016)

We present a new design of a time-preserving extreme-ultraviolet (XUV) monochromator using a semi-infinite gas cell as a source. The performance of this beamline in the photon-energy range of 20 eV to 42 eV has been characterized. We have measured the order-dependent XUV pulse durations as well as the flux and the spectral contrast. XUV pulse durations of ≤ 40 fs using 32 fs, 800 nm driving pulses were measured on target. The spectral contrast was better than 100 over the entire energy range. A simple model based on the strong-field approximation (SFA) is presented to estimate different contributions to the achieved XUV pulse duration. On-axis phase-matching calculations are used to rationalize the variation of the photon flux with generation pressure and intensity.

I. INTRODUCTION

XUV photon sources are powerful tools for probing the electronic structure and dynamics of matter. Continuous light sources and synchrotrons emitting in the XUV to soft X-ray region of the electromagnetic spectrum have been used to conduct photoabsorption, photoionization and photoelectron measurements on a wealth of samples[1–3]. Structurally simple and theoretically accessible systems have been measured in the most meticulous detail, with a recent shift of the focus towards ever more complex objects of interest. With the advent of sufficiently short XUV pulses[4–13], dynamical effects can be examined directly in the time domain revealing new insights into the quantum-mechanical foundations of chemistry and physics. For example time- and angle-resolved photoelectron spectra can be measured providing access to individual partial-wave contributions and their relative phase shifts[14–17]. Together with the recent progress on field-free alignment techniques molecular-frame photoelectron angular distributions can be directly determined. First experimental efforts in this direction have been reported in the ultraviolet spectral range[18].

In this work we present a table-top beamline for the generation of femtosecond XUV pulses based on the principle of high-harmonic generation (HHG)[19–21] and consecutive separation of individual harmonic orders with minimal temporal broadening. High-order harmonics are typically generated by focusing an intense laser pulse onto a gas-phase medium. The first published scheme, which is still widely used today, is loose focusing of the driving laser into a gas jet emerging from a valve[19]. It was found that by considering macroscopic propagation effects during the XUV generation the volume for coherent generation could be increased, thereby increasing the obtained XUV flux[22]. To improve the generation efficiency first variable-length gas cells[23] and later gas-filled hollow-core waveguides[24,25] were used. The method implemented here is known as the semi-infinite gas cell[26–29] where a sharp pressure gradient is created close to the focus. Recent publications indicate excellent generation efficiencies and favorable properties in terms of handling and long-term stability[30]. During HHG a spectral comb of discrete harmonics is created, corresponding to a pulse train in the time domain. Various techniques can be used to isolate specific spectral regions of the generated radiation. Thin metal filters with spectrally selective transmission are readily available, e.g. indium which can be used to select radiation between 12 eV and 17 eV. However, these filters are inherently inflexible in the choice of the spectral window, are delicate to handle and store due to their thickness (typically a few hundred nanometers) and have a tendency to oxidize[31]. Another option are XUV multilayer mirrors[32]. However, these mirrors only reflect within a defined spectral region and the reflectivity is generally low except for specific ranges, e.g. around 90 eV[33]. Multilayer mirrors as well as metal filters have the advantage that they can simultaneously be used for dispersion management[34,35]. Other than selective transmission or reflection, there are various ways to achieve a spatial separation in the XUV, like gratings or Fresnel zone plates[6,13,36–38]. In this work a scheme called conical diffraction[39,40] was chosen, where a commercially-available plane blazed grating is used under grazing incidence with its lines approximately parallel to the propagation direction of the incident light[10,40–42]. This particular design is also referred to as the off-plane geometry. The benefits of conical diffraction are a high diffraction efficiency of up to 40% in the first order[10,43,44], and a low temporal pulse spread[10].

The remainder of this paper is structured as follows. Sections II A through II D focus on the experimental details of the presented work. All following subsections of section II explain the models used to rationalize the results given in section III and to support the conclusions presented in section IV.

II. METHODS

A. Fundamental Light Source

The laser system used for the present experiments is a titanium:sapphire regenerative amplifier system followed by a single-pass amplifier. It delivers 30 fs laser pulses with a pulse energy of 10 mJ at a repetition rate of 1 kHz and a beam diameter of 10 mm. The output spectrum of the system is centered at 800 nm and has a spectral width (FWHM) of 60 nm (0.12 eV). In all experiments a fraction of the laser output was sent through an attenuator based on a half-wave plate and a thin-film polarizer that enabled the pulse energy used for XUV generation to be varied between 0 and 3 mJ.

B. XUV Source

Our XUV source design builds on the principle of the semi-infinite gas cell[28,29,45]. Figure 1 shows the design of the gas cell. The fundamental beam is focused into a volume with a comparably high gas pressure (HP) which ends with a pinhole (P1), being located close to the focus of the laser and separating the high pressure volume from two subsequent differential pumping stages (DP1, DP2). This abrupt change of pressure creates advantageous phase-matching conditions[29] and minimizes reabsorption. A brief discussion of 1D on-axis phase matching in the semi-infinite gas cell for the experimental parameter sets can be found in section II G.

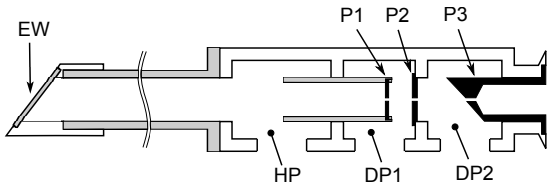

FIG. 1. Schematic drawing of the designed gas cell. The fundamental beam is focused through the entrance window EW such that the focus is located close to pinhole P1. The high-pressure region HP is separated from the experiment by two differential pumping stages DP1 and DP2. The corresponding pinholes are P2 and P3.

The total XUV photoabsorption cross section of the rare gases is highest for photon energies close to the ionization threshold of the particular species[1,46]. It is therefore advantageous to minimize the distance between P1 and P2. In the presented design a helical gear mechanism allows to change this distance between 0 mm and 35 mm. Tab. I gives an overview of the absorption-length-pressure products ξ[47] of the relevant generation gases directly at the ionization threshold.

In the pressure range from 0 to 100 mbar in the HP region, the achieved pressures in DP1 and DP2 are then sufficiently low to disregard absorption effects after the generation. Typical pressures for the differential pumping stage DP1 and DP2 are listed in Tab. II.

gas type	He	Ne	Ar	Kr	Xe
I_p [eV]	24.6	21.6	15.8	14.0	12.1
ξ [mm · mbar]	56	66	13	9.7	6.6

TABLE I. Absorption-length-pressure products for various relevant gases at the ionization threshold. Calculated from data given in Refs.[1,46].

HP [mbar]	DP1 [mbar]	DP2 [mbar]
1	$2.5 \cdot 10^{-2}$	$6.6 \cdot 10^{-6}$
10	$4.9 \cdot 10^{-2}$	$9.8 \cdot 10^{-6}$
100	$29 \cdot 10^{-2}$	$140 \cdot 10^{-6}$

TABLE II. Pressures in the differential pumping stages. The cell was filled with Ar. The measurements have been carried out with a diameter of 0.5 mm for all pinholes and a thickness for P1 and P2 of 3 mm. DP1 was pumped with a 420 l/min scroll pump, DP2 with a 240 l/s turbo-molecular pump. The pressure in HP was regulated with a precision needle valve.

For the ease of optical alignment the cell was machined in such a way that all pinholes and the iris in front of the entrance window are lying on the same axis. A 45-degree mirror can be introduced after the cell to send the fundamental beam through a window allowing to inspect the beam profile and the transmitted power after all pinholes. This is critical for the alignment of the laser beam through the cell as well as to prevent damage to the pinholes. The position of the focus inside the gas cell can be translated relative to the pinhole P1 in order to optimize the flux and the spatial properties of the high harmonics. This is done by either moving the focusing optics or pinhole P1 using the mechanism described above.

Throughout this work the high-harmonic radiation was generated by focusing the fundamental 800 nm beam with a focal length of $f_{foc} = 750$ mm. The beam used for the experiments had a $\frac{1}{e^2}$ diameter of 10 mm. An aperture was used to adjust the intensity in the focus and to clean the spatial profile of the focus. The data presented is measured with an iris diameter of $D_0 = 6$-8 mm. Huygens-Fresnel type calculations were done to estimate the effective spot size of this truncated Gaussian beam (see section II F). For $D_0 = 7$ mm the FWHM spot size was calculated to be 80 μm. Since the beam is propagating a considerable distance in the generation gas before the focal position, the real spot size may be somewhat larger.

C. Monochromator

The optical layout presented in this section closely follows the design proposed in Ref.[10]. We therefore limit our discussion to aspects which are either unique to this work

or necessary for later analysis. Figure 2 shows a conceptual depiction of conical diffraction and defines the angle convention. The high diffraction efficiency of up to 40 % in conical diffraction is achieved for those harmonics, where the reflection from the grating facets points in the direction of the desired diffraction order[39,40,48].

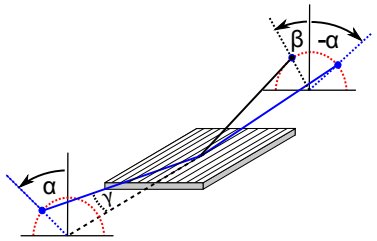

FIG. 2. The conical diffraction scheme: The beam is incident on the grating with its propagation direction almost parallel to the grating lines. γ denotes the angle between the grating lines and the incident beam, α represents the angle between the grating surface normal and the incident beam and β is the diffraction angle.

By rotating the grating around an axis parallel to the grating lines the total diffraction angle $\alpha + \beta$ can be changed and a particular harmonic can be aligned through a selection slit positioned at the intermediate focus after the grating. The required rotation angles for the presented setup are on the order of a few mrad and the variations in the diffraction efficiency can be up to a factor of two in that range[7]. Figure 3 shows the optical layout of the presented monochromator.

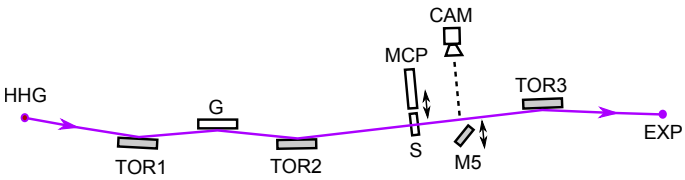

FIG. 3. Optical layout of the monochromator. The XUV beam is collimated by the toroidal mirror TOR1. It propagates onward to the grating G after which it is refocused onto the selection plane by TOR2. The focus in the selection plane is imaged by the mirror TOR3 into the experiment. The selection slit S can be replaced by a multi-channel plate detector (MCP). Via M5 the phosphor screen of the MCP can be imaged with a camera (CAM).

The focal length of TOR1 is 500 mm for geometrical reasons. TOR2 has the same focal length as TOR1 creating a 1:1 image of the XUV generation region in the selection plane. By using the grating equation for the first-order diffraction of a grating in conical diffraction[40],

$$\beta_q = \arcsin\left(\frac{\lambda\Lambda}{\sin(\gamma)} - \sin(\alpha)\right) \tag{1}$$

where Λ denotes the line density of the grating, the estimated spatial separation in the selection plane can be calculated

$$\Delta s = \mathrm{f_{TOR2}} \sin(\gamma)\Delta\beta. \tag{2}$$

With the used 300 lines/mm grating consecutive odd harmonics are well separated up to harmonic 29 of 800 nm for the typical spot sizes obtained in the selection plane (see figure 5). The employed grating has a blazing angle of $\delta = 6.5°$ and a resulting peak efficiency at 27 eV (H17). Gratings with this particular set of parameters are in widespread use for other spectroscopic applications and are therefore readily available.

In the case of a diffraction grating all radiation contributing to the n-th order diffraction experiences an optical path length difference between neighboring lines of $\Delta s = n\lambda$ with n being the diffraction order. The approximate total time spread is then given by

$$\Delta\tau = (N-1)\frac{\lambda_0}{qc}, \tag{3}$$

where N is the number of illuminated lines and q is the order of the generated harmonic. The estimation of the XUV spot size on the grating is not straightforward, since there is no simple dependence of the far-field divergence on the harmonic order. This is because the spatial distribution in the far field is determined by considering a phase-matching problem involving the atomic dipole phase[49]. In section II E we present a simple model to approximate the order-dependent spot size d_q at the position of the grating. The resulting pulse duration is then

$$\tau(q) \approx \tau_0(q) + d_\mathrm{q}\Lambda\frac{\lambda_0}{qc}, \tag{4}$$

where $\tau_0(q)$ is the order-dependent duration of the harmonics immediately after generation. Equation (4) thus shows that the chosen conical-diffraction geometry imparts an order-dependent temporal broadening on the harmonics because of a different number of illuminated grating lines as well as a harmonic-order-dependent time spread per illuminated grating line.

All toroidal mirrors were bought as bare substrates and later coated with a 100 nm thick diamond-like carbon coating by the Swiss Federal Laboratories for Material Science (EMPA). The mirrors are positioned in the beam path under 87° angle of incidence. According to the literature these parameters allow for a mirror reflectivity of $\geq$ 90 % for s- and p-polarization in the range from 30 eV to 100 eV[50,51]. Since the reflectivity is predicted to increase for higher photon energies a reflectivity measurement at 30 eV is sufficient to verify this property. The experimental reflectivity at 32.5 eV was found to be 92% for the polarization being parallel to the plane of incidence on the mirror. In the range from 1 eV to 30 eV the reflectivity is still predicted to be $\geq$ 80 % for s-polarization

but drops down to about 60 % for p-polarization[52]. The grating is a standard plane ruled replica grating with a bare gold coating. The value of 40 % diffraction efficiency given in the introduction was measured for this type of grating[10,43,44]. According to the values given here, the total transmission of the monochromator as shown in figure 3 is on the order of 30 % above 30 eV.

Two features are essential for the operation of the monochromator. The first is a multi-channel-plate detector (MCP) which can be introduced in the selection plane to observe the incident XUV radiation. It allows for the optimization of high-harmonic generation in the gas cell without being dependent on an alignment-critical experiment. Figure 4 displays an example image of the MCP taken by a camera.

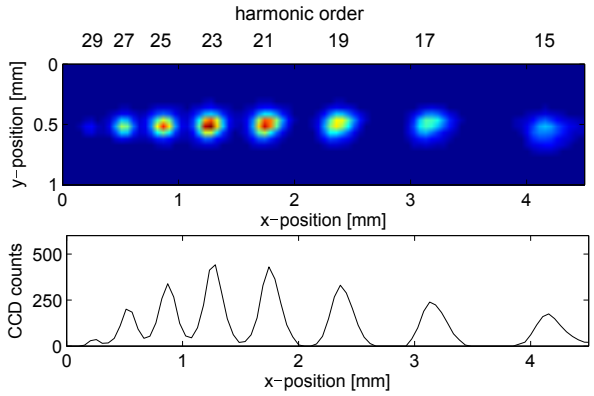

FIG. 4. Image taken from the MCP in the selection plane. The XUV radiation was generated by focusing 1.5 mJ into the gas cell filled with 20 mbar argon. Top: Image taken directly from the MCP. Bottom: Integral of the image along the y-axis.

It is important that the individual spots have a symmetric shape because under some conditions the XUV can broaden spectrally[45] leading to overlap between the individual harmonic orders. Figure 5 shows the full-width at half maximum (FWHM) of the individual harmonics as well as their individual separation, justifying the choice of a 300 μm selection slit. The second crucial feature is the possibility to rotate the grating such that the zero order reflection of the fundamental can be guided through the rest of the setup. In this way the monochromator can be aligned with the vacuum chambers vented.

The setup including the semi-infinite gas cell is mounted on an optical table with dimensions 800 mm × 2400 mm. The vacuum part of the beamline was split into three separate chambers all being based on standard vacuum components. The first chamber (DN400) is housing TOR1, TOR2 and the three axis goniometer holding the grating G. The second and third chambers (DN250) house the MCP-selection-slit assembly and

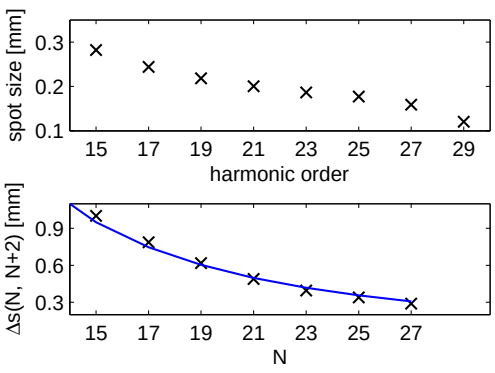

FIG. 5. Measured spatial properties of the harmonics in the separation plane. Top: FWHM spot size obtained by Gaussian fit. Bottom: Spatial separation Δs between consecutive odd harmonic orders. The blue line corresponds to equation (2) for the experimental parameters: $\Lambda = 300\,\mathrm{l/mm}$, $\gamma = 3.5°$, $\alpha = 6.5°$ and $f_{\mathrm{TOR2}} = 500\,\mathrm{mm}$.

TOR3, respectively.

D. Detectors

All measurements of photon flux have been done with a calibrated XUV photodiode with a 100 nm aluminium layer directly deposited on the diode, blocking stray light of the fundamental and all harmonic orders below 15 eV. Within a day of exposure to atmosphere a stable oxide layer forms on any bare aluminium surface[31], reducing the conversion efficiency of the diode. As it is not possible to entirely avoid any exposure of the diode to air, all values measured here should be considered as a lower bound to the actual photon flux. The real values may be higher due to the fact that the calibration curve was measured without oxide layer.

A magnetic-bottle-photoelectron spectrometer (MBES) was used for the cross-correlation measurements, the assignment of the individual harmonic orders as well as the estimation of the residual transmission of neighboring harmonics. An extensive description of this MBES can be found elsewhere[53]. The quantum efficiency of the implemented MCP peaks around 500 eV[54] and decreases rapidly towards 10 eV. By adding a mesh on the front surface of the MCP assembly an acceleration potential was applied to allow for a more homogeneous collection efficiency of the slow electrons. The MCP output is directly wired to a wide-band-small-gain amplifier which is read out with a time-to-digital converter.

The pulse duration of the generated XUV pulses was quantified in a small-angle non-collinear pump-probe geometry as depicted in figure 6. Before the XUV gen-

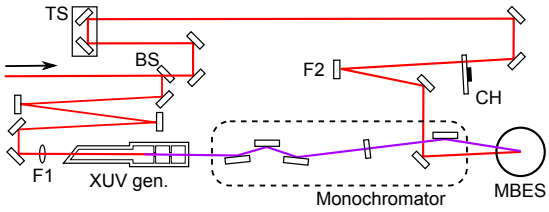

FIG. 6. Sketch of the setup used for the pulse duration characterization. The beamsplitter BS is used to separate the incoming IR radiation in two interferometric arms. The majority of the power is focused with the lens F1 into the semi-infinite gas cell for XUV generation and consecutive monochromatization. The resulting radiation is combined with the remaining IR in the MBES. Before focusing the IR via F2, a chopper CH is employed to block every second pulse thereby allowing for single-shot-referenced detection. The optical path length of the IR pulses could be changed using a motorized translation stage TS.

eration 100 μJ were split off the fundamental IR beam. This light was then focused with a focal length of 1 m into the interaction region of the MBES where it crossed the XUV beam at an angle of 3 °. Spatial and temporal overlap of the XUV and IR pulses leads to the appearance of sidebands at kinetic energies both above and below the XUV-induced photoelectrons. At low IR intensities these photoelectrons correspond to two-photon ionization pathways. In this case the electron count rate of the sideband photoelectrons is proportional to the product of the intensity envelopes of the XUV and IR pulses. By scanning the temporal delay between the two light pulses an envelope cross-correlation can be obtained[55,56]. For all measurements the maximal height of the sidebands was set to a value of 5-10 % of the main peak height as under these conditions no second order sidebands could be observed. The height of the sidebands was set by changing the IR intensity in the focal region with an iris placed in the beam path before the focusing mirror. Backfilling of the interaction region with argon gas to a pressure of 5×10^{-5} mbar served as target for photoionization.

To extract the duration of the XUV pulse, the IR pulse was characterized via an interferometric auto-correlation and the FWHM of the envelope was determined to be 32 fs. Assuming the XUV pulse and the IR pulse to have a Gaussian temporal shape, the temporal width can be calculated from the cross-correlation and the envelope of the IR:

$$\sigma_{\mathrm{XUV}} \approx \sqrt{\sigma^2_{\mathrm{x-corr}} - \sigma^2_{\mathrm{IR}}}. \tag{5}$$

The results of these measurements are shown in figure 17.The measured pulse durations are found to generally decrease with increasing harmonic order. At least two possible origins of this effect can be identified. First, the divergence of the high-harmonic beam and thus the number of illuminated grating lines decreases with increasing harmonic order. This effect was discussed in section II C. Second, the generation mechanism itself may cause this effect, which we study in the following section (II E).

E. Temporal Emission Profile

To quantify the effects of the HHG process itself on the expected pulse duration the single-atom response of the sample gas in the presence of the driving laser pulse was calculated using the semi-classical strong-field approximation[21]. The implementation presented here closely follows Ref.[57] without the phase matching part presented there. Since the majority of the steps are explained in great detail in the aforementioned reference, we will give only as much of a description as is necessary to explain aspects where our treatment differs. All equations in this subsection will be given in atomic units. The fundamental laser field is assumed to be of the form

$$E_{\mathrm{L}}(t) = E_0 A(t) \cos(\omega_{\mathrm{L}} t), \tag{6}$$

where E_0 is the peak amplitude of the field, $A(t)$ is an envelope function being normalized to a maximal value of one and ω_L being the angular center frequency of the laser. For all calculations shown $A(t)$ was assumed to be of Gaussian shape being uniquely defined by the given FWHM pulse duration τ. The starting point for the SFA calculations is the induced time-dependent dipole moment written as

$$d(t) = \mathrm{Re}\left[\exp\left(-i\frac{\pi}{4}\right) \sum_{\mathrm{traj.}} a_{\mathrm{i}}(t)\, a_{\mathrm{p}}(t)\, a_{\mathrm{r}}(t)\right], \tag{7}$$

with $a_{\mathrm{i}}(t)$ containing the complex ionization amplitude, $a_{\mathrm{p}}(t)$ the propagation phase and $a_{\mathrm{r}}(t)$ the complex recombination amplitude of the trajectories recombining at time t. Using two consecutive saddle-point approximations a connection between the quantum-mechanical behavior and classical trajectories can be established[21,58]. For these classical trajectories there is a unique mapping between birth times t_{b} and recombination times t_{r}, provided that the initial velocity of the electron $p(t_{\mathrm{b}})$ is 0. This implies

$$d(t) = \sum_{\mathrm{hc}} d_{\mathrm{hc}}(t_{\mathrm{r}}) \tag{8}$$

and

$$d_{\mathrm{hc}}(t_{\mathrm{r}}) = \mathrm{Re}\left[\exp\left(-i\frac{\pi}{4}\right) a_{\mathrm{i}}(t_{\mathrm{b}})\, a_{\mathrm{p}}(t_{\mathrm{b}}, t_{\mathrm{r}})\, a_{\mathrm{r}}(t_{\mathrm{r}})\right], \tag{9}$$

where d_{hc} is the half-cycle induced dipole moment. The expressions above can be easily evaluated since the

function $t_\mathrm{b}(t_\mathrm{r})$ can be obtained classically. The nonlinear map between t_b and t_r leads to the problem that the integrated half-cycle ionization probability $a_\mathrm{hc} = \int_\mathrm{hc} a_\mathrm{i}(t_\mathrm{b})\mathrm{d}t_\mathrm{b}$ is not equal to $a_\mathrm{hc} = \int_\mathrm{hc} a_\mathrm{i}(t_\mathrm{b}(t_\mathrm{r}))\mathrm{d}t_\mathrm{r}$. This is accounted for by introducing the corresponding Jacobi correction. Therefore

$$a_\mathrm{i}(t_\mathrm{r}) = \frac{\mathrm{d}t_\mathrm{b}}{\mathrm{d}t_\mathrm{r}} \sqrt{\frac{\mathrm{d}}{\mathrm{d}t} n(t_\mathrm{b})}, \tag{10}$$

where $n(t_\mathrm{b})$ is the probability that an initially neutral atom is ionized at t_b. Deviating from Ref.[57] nonadiabatic tunnel ionization rates[59] have been used to calculate $n(t_\mathrm{b})$. The propagation term used here is

$$a_\mathrm{p}(t_\mathrm{r}) = \left(\frac{2\pi}{t_\mathrm{r} - t_\mathrm{b} + \epsilon}\right)^{3/2} \frac{(2I_\mathrm{p})^{1/4}}{|E_\mathrm{L}(t_\mathrm{b})|} \times \exp\left(-i\left(t_\mathrm{r} - t_\mathrm{b}\right) I_\mathrm{p} - iS\left(t_\mathrm{r}\right)\right), \tag{11}$$

where $E_\mathrm{L}(t_\mathrm{b})$ is the electric field of the laser at the time of birth, I_p is the ionization potential and $S(t_\mathrm{r})$ represents the action accumulated along the classical trajectory. Here ϵ was introduced to prevent $a_\mathrm{p}(t_\mathrm{r})$ from diverging for $t_\mathrm{r} - t_\mathrm{b} = 0$ which happens for the trajectories born right at the zero crossing of the electric field. For all simulations presented ϵ was set to 2π setting the prefactor to 1 for $t_\mathrm{r} - t_\mathrm{b} = 0$. The recombination dipole was calculated using the approach described in Ref.[60]. Therefore

$$a_\mathrm{r}(t_\mathrm{r}) = \sqrt{n(t_\mathrm{r})} d_\mathrm{el}\left(p_\mathrm{r}^2(t_\mathrm{r})\right), \tag{12}$$

where $d_\mathrm{el}\left(p_\mathrm{r}^2(t_\mathrm{r})\right)$ represents the energy-dependent recombination dipole. We have approximated the electron energy with the kinetic energy $E_\mathrm{kin} = p_\mathrm{r}^2(t_\mathrm{r})$ with p_r being the classical momentum of the electron at recombination.

The SFA implemented as described will result in the combined dipole moment of all sub-cycles containing discontinuities at the positions of $t_\mathrm{r} - t_\mathrm{b}$. This leads to a situation where the calculated spectra $d(\omega) = \mathcal{F}(d(t))$ are dominated by Fourier components of these artifacts. This is a known issue caused by the second saddle point approximation and the implicit assumption of a negligible electron momentum at birth time. This can be seen from the condition for the second saddle point[59]

$$\left[p_\mathrm{b} - \sin(\omega_\mathrm{L} t_\mathrm{b}) + \sin(\omega_\mathrm{L} t_\mathrm{r})\right]^2 + \gamma^2 = 0, \tag{13}$$

where p_b is the classical momentum at birth time and γ is the Keldysh parameter[61]. Obvious limitations arise from the fact that the classical picture can only be recovered for $p_\mathrm{b} \ll 1$ and for $\gamma^2 \approx 0$ which is hardly ever realized under realistic experimental conditions. Assuming $\gamma^2 = 0$ and $p_\mathrm{b} \ll 1$ there are still two issues, first, the existence of two solutions to equation (13) in each half cycle, and second, the fact that for very short trajectories

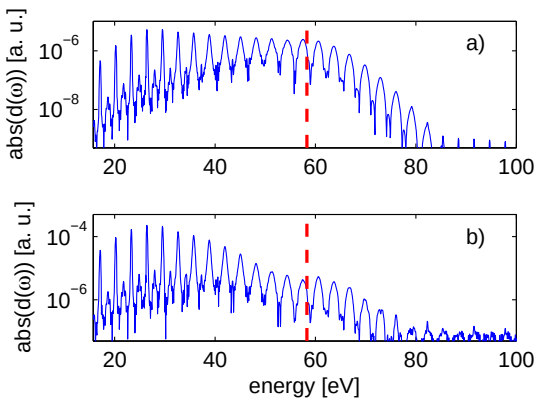

FIG. 7. Absolute values of the spectral dipole response for HHG from argon ($I_\mathrm{p} = 15.7\,\mathrm{eV}$) using a 32 fs pulse centered at 800 nm with a peak field strength of 0.08 a. u.. a) $\sigma_\mathrm{f1} = 0.25\frac{1}{f_\mathrm{L}}$, $\sigma_\mathrm{f2} = 0.1\frac{1}{f_\mathrm{L}}$ and $d_{el} = 1$. b) same as a, but $d_{el} = d_{el}^{Ar}$. The red line indicates the cutoff at $3.17U_\mathrm{p} + I_\mathrm{p}$. The Cooper minimum at 53 eV[60] appears around 55 eV, being shifted towards higher energies as a consequence of its proximity to the cutoff.

where $t_\mathrm{b} \approx t_\mathrm{r}$ the assumption $p_\mathrm{b} \approx 0$ becomes insufficient. It is common practice to deal with these issues by introducing a filter which suppresses one of the two solutions and a second filter which suppresses trajectories corresponding to very short transit times. The application of the second saddle point is also the reason why the behavior of this SFA implementation differs from the one presented in Ref.[21] in so much as for the present work $d(\omega)$ decreases towards energies close to the I_p while it shows the opposite behavior in the original publication.

The filter suppressing very short trajectories was chosen as follows

$$a_\mathrm{f1}(t_\mathrm{r}) = 1 - \exp\left(-\frac{(t_\mathrm{r} - t_\mathrm{b})^2}{\sigma_\mathrm{f1}^2}\right), \tag{14}$$

where we set $\sigma_\mathrm{f1} = 0.25\frac{1}{f_\mathrm{L}}$ with f_L being the fundamental laser frequency. For smaller σ_f1 the spectrum starts to be dominated by the corresponding frequency components of the filter while larger values only result in an overall reduction of the dipole response.

The two different solutions to equation (13) can be identified as the long and short trajectories which are separated by the maximum in recollision momentum. The trajectories towards shorter recollision times are the short trajectories and the ones towards longer recollision times are the long trajectories. Here we determine the time t_rm corresponding to the maximal recollision momentum and apply an edge filter which suppresses contributions to $d(t)$ from longer recollision times

$$a_{\mathrm{f2}}(t_\mathrm{r}) = \frac{1}{2}\left[1 - \mathrm{erf}\left(\frac{t_\mathrm{r} - t_\mathrm{rm}}{\sigma_{\mathrm{f2}}}\right)\right], \tag{15}$$

where $\sigma_{\mathrm{f2}} = 0.1\frac{1}{f_\mathrm{L}}$. Similar to the first filter smaller σ_{f2} generate artificial high-frequency components while larger values lead to less suppression. The final expression for the half-cycle response is then

$$d_{\mathrm{hc}}(t_\mathrm{r}) = \mathrm{Re}\Big[\exp\left(-i\frac{\pi}{4}\right) a_\mathrm{i}(t_\mathrm{r})\, a_\mathrm{p}(t_\mathrm{r}) \times a_\mathrm{r}(t_\mathrm{r})\, a_{\mathrm{f1}}(t_\mathrm{r})\, a_{\mathrm{f2}}(t_\mathrm{r})\Big]. \tag{16}$$

When including the two filter functions the wavelength and intensity scaling of the cutoff is reproduced as well as the Cooper minimum in argon (see Fig. 7). The above formalism allows us to calculate individual half-cycle spectra. Disregarding phase-matching effects the temporal envelope of each harmonic order is calculated by evaluating the envelope of the spectral dipole response as a function of the individual half cycles.

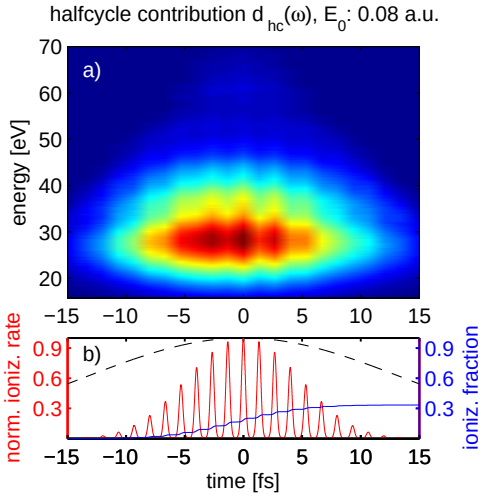

FIG. 8. Calculated half-cycle contributions $d_{\mathrm{hc}}(\omega)$ for HHG in argon using a 32 fs pulse centered at 800 nm and a peak electric field of $E_0 = 0.08$ a. u.. For each half cycle about 2^{14} trajectories have been calculated. The lower panel shows the normalized ionization rate, the total ionization fraction and the envelope of the fundamental laser field (dashed black curve).

Figure 8 shows the calculated half-cycle spectrum for argon for an experimentally relevant parameter set. For energies below about 30 eV the calculated behavior is unphysical as the observed temporal width of the emission dipole is decreasing. We attribute this effect to the set of problems stemming from the second saddle point and therefore, from this point on, show only the results obtained above 30 eV (or H17). Figure 9 shows the FWHM of a Gaussian fit to the individual half-cycle contributions of different harmonics. The mentioned change in the overall trend is clearly visible.

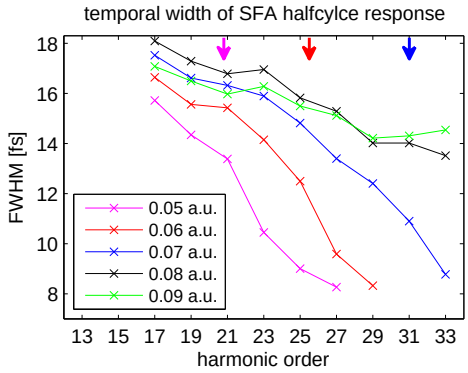

FIG. 9. The temporal width of the individual harmonics obtained by a Gaussian fit to the half-cycle map from Fig. 8. As expected the temporal duration decreases with increasing harmonic order as well as with decreasing field strength. The harmonics in the cutoff show a significant decrease in pulse duration. For $E_0 = 0.05,\ 0.06,\ 0.07$ a. u. the cutoff is at harmonic order 20.8, 25.5, 31.1 respectively (indicated by arrows). For $E_0 = 0.09$ a. u. significant ionization depletion occurs which explains the reduced effective pulse duration. We only show the experimentally relevant harmonic orders.

F. 1D XUV Far-field Profile

Neglecting all further propagation effects and assuming an infinitesimally thin generation region located in the focal plane, the spatial profile of the harmonics on the grating surface can be estimated. For spectrally well seperated harmonics or in the absence of nonlinear propagation effects the linearized Born approximation[62,63] describes the field propagation of the harmonics

$$\nabla^2 \vec{E}_\mathrm{q}(\omega) + \frac{\omega^2}{c^2} n_\mathrm{q}^2 \vec{E}_\mathrm{q}(\omega) = -4\pi \frac{\omega^2}{c^2} \vec{P}_\mathrm{q}^{\mathrm{nl}}(\vec{E}_\mathrm{F}, \omega) \tag{17}$$

where $\vec{E}(\omega)$ describes the electric field of the harmonic in the frequency domain, ω is the angular frequency, n_q the refractive index and $\vec{P}_\mathrm{q}^{\mathrm{nl}}(\vec{E}_\mathrm{F}, \omega)$ is the nonlinear polarization induced by the fundamental beam. Hence for an infinitesimal generation region and a single polarization

$$E_\mathrm{q}(\omega) \propto -P_\mathrm{q}^{\mathrm{nl}}(E_\mathrm{F}, \omega) \propto -d(\omega) \approx -d(\omega_q). \tag{18}$$

Using the equation above, a simple 1D Huygens-Fresnel calculation can be performed treating the beam as quasi monochromatic. Let z be the direction of beam propagation and x be a dimension perpendicular to z. We start with a far-field profile $E_\mathrm{F}(x, z_s)$ which represents the truncated Gaussian spatial profile used in the experiment (see section II B). To emulate the focusing lens the initially assumed flat phase is multiplied with the phase factor corresponding to a flat lens[64]

$$f_{\mathrm{lens}}(x) = \exp\left(i\frac{k}{2f_{\mathrm{foc}}}x^2\right). \tag{19}$$

This profile is then propagated to the focal plane with a numerical implementation of the Huygens Fresnel integral

$$E(\omega, x, z_2) \propto \int E(\omega, x', z_1) \times \exp\left(-ik(\omega)\sqrt{\delta_z^2 + (x - x')^2}\right) \mathrm{d}x', \quad (20)$$

with $\delta_z = z_2 - z_1$. In order to compare the results to the previous section the obtained field distribution in the focus $E(x, z_f)$ is then renormalized to E_m. It can be shown that equation (20) is a limiting case of the Green's function solution to equation (17)[62,65]. Having calculated the spatial distribution in the focal plane, the nonlinear response can be calculated using the SFA formalism from section II E to obtain $E_q(x, z_f)$. Figure 10 shows the electric-field distribution of the fundamental and of an exemplary harmonic.

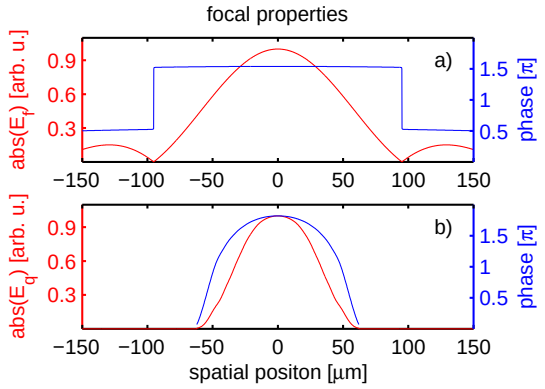

FIG. 10. Panel a) shows the absolute value and phase of the electric field of the fundamental beam in the focal plane. Panel b) shows the same properties for H21 calculated for E_m = 0.08 a. u..

Applying equation (20) a second time to the calculated harmonic field, the spatial property of different harmonics in the grating plane can be estimated. A significantly more elaborate but similar implementation taking into account the cylindrical symmetry of the problem and assuming a finite generation volume can be found in Ref.[49]. The results of our calculations are shown in figure 11. Together with the results displayed in figure 9 we can use equation (4) to estimate the effective pulse duration of the XUV after monochromatization.

G. On-axis Phase Matching in the Semi-Infinite Gas Cell

An extensive discussion of phase-matching of high-order harmonics in a semi-infinite gas cell can be found in Ref.[29]. A general treatment including a more complete derivation of the used formalism is found in Refs.[22,47,62,66]. We restrict our treatment to one dimension which is chosen to be the laser propagation direction

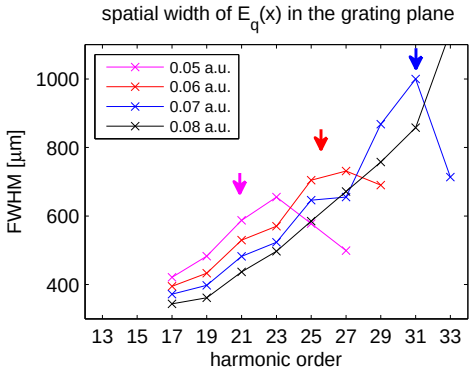

FIG. 11. Calculated spatial width of the individual harmonics in the grating plane. The overall behavior is similar for all four calculated values of the peak electric field E_m. The harmonic orders in the vicinity of the cutoff (indicated by arrows) decrease in width as expected.

and we only discuss argon as a generation medium. It is important to point out that a very similar treatment of 1-D phase-matching in absorbing gases can be found in Ref.[67] which was used for the evaluation of phase matching in the semi-infinite gas cell in Ref.[30]. In the case of linear polarization and neglecting diffraction effects, the wave equation (17) can be rewritten as

$$\frac{\partial^2}{\partial z^2} E_\mathrm{q}(\omega, z) + \frac{\omega^2}{c^2} n(\omega_q, z)^2 E_\mathrm{q}(\omega, z) = -4\pi \frac{\omega^2}{c^2} P_q^\mathrm{nl}(E_\mathrm{F}(z), \omega), \quad (21)$$

where z is the propagation direction of the fundamental laser beam. Equation (21) has the solution[62,68]

$$E_q(\omega_q, z) = \left(\frac{\omega_q}{c}\right)^2 \int_{-\infty}^{z} \rho(z') P_q^\mathrm{nl}\left(E_\mathrm{F}\left(z'\right), \omega_q\right) \times \frac{1}{z - z'} \exp\left(-i\phi_q(z')\right) \mathrm{d}z', \quad (22)$$

where $\rho(z)$ is the spatially dependent generation gas density and $\phi(z')$ is given by

$$\phi_q(z') = \int_{z'}^{z} k_q(z'') - i\alpha_q(z'') \, \mathrm{d}z'', \quad (23)$$

with $k_q(z) = \mathrm{Re}(\frac{\omega_q}{c} n(\omega_q, z))$ and $\alpha_q(z) = \mathrm{Im}(\frac{\omega_q}{c} n(\omega_q, z))$. We assume for simplicity that

$$\alpha_q(z) = \frac{\rho(z)}{\rho_\mathrm{ref}} \alpha_\mathrm{ref}(\omega_q) = \frac{p(z)}{\xi(\omega_q)}, \quad (24)$$

where α_ref is an experimental reference absorption length measured at the reference particle density ρ_ref

and $\xi(\omega_q)$ is the absorption-length-pressure product introduced in section II B. For the spatially dependent refractive index $n_{\mathrm{F}}(\omega, z)$ we assume that

$$n_{\mathrm{F}}(\omega, z) = \sqrt{1 + \chi_{\mathrm{n}}(\omega, z) + \chi_{\mathrm{el}}(\omega, z)}, \tag{25}$$

where $\chi_{\mathrm{n}}(\omega, z)$ and $\chi_{\mathrm{el}}(\omega, z)$ are the electric susceptibilities of the neutral gas and the free electrons, respectively. In principle, equation (25) should include a third term $\chi_{\mathrm{ion}}(\omega, z)$ which contains the contribution to the refractive index due to the generated ions. This term is however typically neglected. We assume the following form for the neutral gas susceptibility:

$$\chi_{\mathrm{n}}(\omega, z) = \frac{\rho(z)}{\rho_{\mathrm{ref}}}(n_{\mathrm{ref}}(\omega)^2 - 1)(1 - \eta(z)), \tag{26}$$

where $n_{\mathrm{ref}}(\omega)$ is a reference refractive index measured at a reference particle density ρ_{ref} and $\eta(z)$ is the spatially dependent ionization fraction. Due to the absence of tabulated experimental values of $n_{\mathrm{ref}}(\omega)$ in the relevant experimental range it is a viable strategy to calculate this quantity from absorption measurements using the Kramers-Kronig dispersion relation[69]. Since the accurate numerical evaluation of the Kramers-Kronig transforms is nontrivial[70] we resorted to interpolate the data given in Ref.[69]. This approach however neglects the influence of the autoionizing resonances converging to the $(3s)^{-1}$ ionization threshold of argon in the region between 25 and 31 eV[71]. Since Ref.[69] omits this specific energy region, the refractive index for H19 was approximated with a cubic spline fit. The resulting refractive indices for H19 and H21 are $n_{\mathrm{ref}}^{19} = 1 - 2.8\times10^{-4}$ and $n_{\mathrm{ref}}^{21} = 1 - 1.9\times10^{-4}$.

We calculate the ionization fraction $\eta(z)$ by taking its value obtained at the end of the laser pulse with the procedure described in section II E. The free-electron dispersion is approximated by the Drude model[29,72,73]. If the fundamental laser frequency is much higher than the associated plasma frequency, the electric susceptibility of the plasma is given by

$$\chi_{\mathrm{el}}(\omega, z) = -\rho(z)\eta(z)4\pi\frac{1}{\omega^2}. \tag{27}$$

The challenge remaining to obtain $E_q(\omega_q, z)$ is to find a suitable description for $P_q\left(E_{\mathrm{F}}\left(z'\right), \omega_q\right)$. Since we can calculate the dipole response for a given electric field $E_{\mathrm{F}}(t)$ (see section II E), the task is to find $E_{\mathrm{F}}(t, z')$ which can be done by finding the solution of the associated wave equation

$$\frac{\partial^2}{\partial z^2}E_{\mathrm{F}}(\omega, z) + \frac{\omega^2}{c^2}n(\omega, z)^2 E_{\mathrm{F}}(\omega, z) = 0. \tag{28}$$

We have implicitly neglected the nonlinear polarization since finding a solution for the non-linear wave equation is complicated and advanced numerical calculations are necessary. Therefore, we only include the spatial dependence of the refractive index $n_{\mathrm{F}}(\omega_{\mathrm{F}}, z)$ and neglect the remaining nonlinear effects. In Ref.[74] an empirical formula can be found for the refractive index of argon at 1013.25 mbar in the range of 140.4 to 253.7 nm. We use this expression to calculate $n_{\mathrm{F}}(\omega_{\mathrm{F}})$ after having cross checked the predicted values at 826.7 nm[75] and found good agreement. The solution to equation (28) is consequently[62,68]

$$E_{\mathrm{F}}(\omega_{\mathrm{F}}, z) = E_{\mathrm{F}}(\omega_{\mathrm{F}}, z_0) \times \exp\left(-\int_{z_0}^{z} ik_{\mathrm{F}}(z')\,\mathrm{d}z'\right), \tag{29}$$

where $k_{\mathrm{F}}(z)$ is defined as $k_{\mathrm{F}}(z) = \mathrm{Re}(\frac{\omega_q}{c}n_{\mathrm{F}}(\omega_F, z))$. Due to the one-dimensional nature of our model, the geometric-phase effect (Gouy phase) is not naturally present. We can however introduce it by rewriting equation (29) using the known properties of a Gaussian beam:

$$E_{\mathrm{F}}(\omega_{\mathrm{F}}, z) = E_0\left(\sqrt{1 + \frac{(z - z_{\mathrm{foc}})^2}{z_{\mathrm{ray}}^2}}\right)^{-1} \times \exp\left(i\xi(z)\right)\int_{z_0}^{z}\exp\left(-ik_{\mathrm{F}}(z')\right)\mathrm{d}z', \tag{30}$$

where we have introduced the on-axis Gouy phase shift $\xi(z) = \arctan(\frac{z - z_{\mathrm{foc}}}{z_{\mathrm{ray}}})$ with z_{foc} and z_{ray} being the focus position and the Rayleigh length respectively[64]. This expression for the Gouy phase is strictly valid for Gaussian beams and therefore can only be taken as an approximation in this discussion.

For all following calculations we have assumed a Gaussian beam with a far-field divergence angle $\theta_0 = 5$ mrad. For a center wavelength of 800 nm this results in a spot size of $2w_0 = 102$ μm and a corresponding Rayleigh length of $z_{\mathrm{ray}} = 10.1$ mm. The numerical evaluation of Equation (22) can be done by using the fact, that due to the absorption of the generated harmonic radiation the integral boundary at $-\infty$ can be replaced by $z^{(-)}$, where $z^{(-)}$ has to fulfill the condition $\left|\rho(z)P_q^{\mathrm{nl}}(z)\exp\left(-i\phi_q(z)\right)\right| \approx 0\ \forall\ z \leq z^{(-)}$. The grid boundary towards negative z is therefore determined by several things: The longest absorption length of the considered harmonics at the lowest considered pressure, by the extent of the generation medium, and by the region where $P_q^{\mathrm{nl}}(z) \neq 0$. For the majority of our simulations the most restricting factor was the absorption length and given the investigated parameter space a grid from $-3z_{\mathrm{ray}}$ to z_{ray} in 2^{11} steps was sufficient to evaluate Equation (22).

The most accessible test piece for this type of code is the reproduction of Maker fringes[76]. If the coherence length L_{coh} is shorter than the effective absorption length L_{abs} an oscillation in the calculated flux as a function of the generation length L_{gen} is expected. The coherence

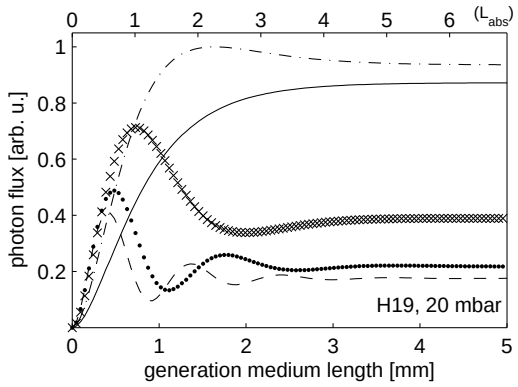

FIG. 12. Calculation of the harmonic flux as a function of generation length $L_{\rm gen}$. The individual curves were calculated for $E_0 = 0.08$ and $z_{\rm foc} = 0$ (dashed), 2 (dotted), 4 (crossed), 6 (dash-dot) and 8 (full) mm resulting in an estimated-coherence length at the exit of the medium of $L_{\rm coh}$ = 0.14, 0.17, 0.26, 0.54 and 7 mm, respectively The absorption length at a pressure of 20 mbar for H19 in argon is 0.7 mm.

length is defined as the length where the spatially dependent phase mismatch of the generation (see Fig. 15) is smaller than π radians and the absorption length is defined as $L_{\rm abs} = 1/\alpha$. Maker fringes have been observed in XUV generation by HHG[77] and have already been theoretically discussed for HHG in absorbing media[67]. In Fig. 12 simulations are presented where a changing generation length is realized by taking a pressure profile given as $p(z) = p_0$ for $z \in [-L_{\rm gen}, 0]$ and $p(z) = 0$ otherwise. The coherence length is varied by changing $z_{\rm foc}$. Having a slightly different range of acessible ratios of $L_{\rm coh}$ to $L_{\rm abs}$ than in Ref.[67] the overall behavior presented there is well reproduced. The different slopes for small values of $L_{\rm gen}$ are due to the fact that by changing $z_{\rm foc}$ the effective maximum field strength in the generation medium is reduced and so is the absolute value of $P_q^{\rm nl}$.

The equations given in this subsection all depend on the spatial variation of the pressure. In Ref.[29] an abrupt transition into vacuum was considered. Precise calculations on the pressure distribution are however difficult since the pressure regime covers the full transition from viscous to molecular flow. As shown in Figs. 13 and 14 c) the variation of the pressure has a quite significant influence on the refractive index of the fundamental and therefore on the outcome of the phase-matching calculations. We approximate the transition from the high-pressure region to the vacuum with an error function

$$p(z) = \frac{p_0}{2}\left[1 - \mathrm{erf}\left(\frac{z}{\sigma_{\rm ph}}\right)\right], \qquad (31)$$

where $\sigma_{\rm ph} = 1.5$ mm is used to approximate the width of the pinhole (3 mm). The pressure is then continuously differentiable and has an almost linear part in the area of the pinhole, which would be expected from laminar flow calculations.

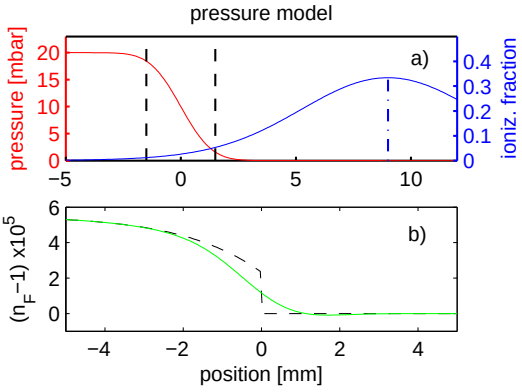

FIG. 13. Panel a) shows the used pressure model. The black dashed lines indicate the dimension of the pinhole, the given ionization fraction is shown for $z_{\rm foc} = 9$ mm (blue dash-dot line) and was calculated for $E_0 = 0.08$ a. u.. Panel b) displays the variation of $n_{\rm F}(z)$ for the pressure given in panel a). For comparison the variation of $n_{\rm F}(z)$ was also calculated for an edge like pressure dependence (dashed black line).

For a qualitative discussion of the results, we rewrite equation (22) in the following way

$$E_q(\omega_q, z) = \left(\frac{\omega_q}{c}\right)^2 \int_{-\infty}^{z} \tilde{P}_q(z') \exp\left(i\tilde{\phi}_q(z')\right) \mathrm{d}z', \qquad (32)$$

where $\tilde{P}_q(z')$ is the absolute value of the initial integrand and $\tilde{\phi}_q(z')$ the corresponding argument.

This has the advantage that phase matching can be discussed by analyzing the phase term $\tilde{\phi}_q(z')$. The quantity $\Delta k_q = -\frac{\partial}{\partial z'}\tilde{\phi}_q(z')$ is often used to quantify the phase mismatch, however we have omitted the discussion of Δk_q and its individual constituents for brevity. Figure 14 shows the calculated variation in harmonic intensity as a function of the focus position relative to the position of the pinhole at a pressure of 20 mbar. Panel a) shows the result for perfect phase matching whereas panel b) includes the calculated phase mismatch. The expected strong phase-mismatch at the position of the focus, as well as the increase of this effect for increasing intensities and hence higher ionization fractions is well reproduced. We also see the expected harmonic-order dependent phase-matching phenomena.

To illustrate the phase-matching argument, Fig. 15 shows $\tilde{\phi}_{19}(z')$ and $\tilde{P}_{19}(z')$ at two different focus positions for $E_0 = 0.08$ a. u.. At the first position ($z_{\rm foc} = +9$ mm), $\tilde{\phi}_{19}(z')$ is almost constant over the entire relevant range. The integral in equation (32) will therefore assume a value close to the phase-matching limit. At the second position ($z_{\rm foc} = 0$ mm) however $\tilde{\phi}_{19}(z')$ varies by several radians over the relevant range of z'. The integral will therefore be comparably small, and depending on the exact set of parameters even close to 0.

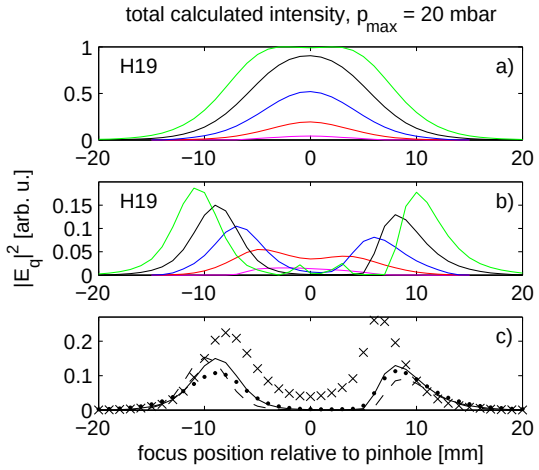

FIG. 14. Panel a) shows the total calculated intensity as a function of the focus position, assuming perfect phase matching ($\tilde{\phi}(z') = 0$) for H19 at various E_0. The distinct shape for $E_0 = 0.09$ (green) is due to ionization saturation. Panel b) shows the intensity variation of H19 including the calculated phase factor $\tilde{\phi}(z')$. Panel c) shows the calculated intensity variation for $E_0 = 0.08$ a. u. for H17 (dotted line), H19 (full line), H21 (dashed line) and H19 calculated for the edge like pressure profile (crossed). The color code for panel a) and b) is identical as in figures 9 and 11. All values for $|E_q|^2$ are normalized to the peak value in panel a).

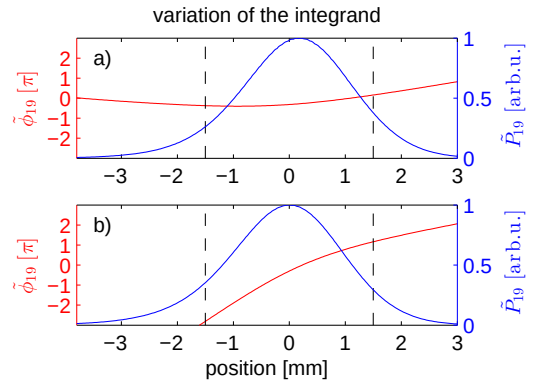

FIG. 15. Panel a) shows $\tilde{\phi}_{19}(z')$ and $\tilde{P}_{19}(z')$ at $z_{\mathrm{foc}} = +9$ mm for $p_0 = 20$ mbar and $E_0 = 0.08$ a. u.. Panel b) shows the same quantities at $z_{\mathrm{foc}} = 0$ mm. The drop of $\tilde{P}_{19}(z')$ towards smaller values of z' is due to absorption in the medium whereas the decrease in $\tilde{P}_{19}(z')$ for bigger values of z' is due to the decrease in gas density. The dashed black lines denote the position of the pinhole.

H. Experimental Field Strength

In order to relate our calculations to the experiments, the experimental field strength has to be estimated. The typical approach is to assume that the intensity distribution is of Gaussian shape in space and time. Assuming radial symmetry this means that

$$I(r,t) = I_0 \exp\left(-4\ln(2)\frac{r^2}{\sigma^2_{\mathrm{FWHM}}}\right) \times \exp\left(-8\ln(2)\frac{t^2}{\tau^2_{\mathrm{FWHM}}}\right), \tag{33}$$

where I_0 is the peak intensity, σ_{FWHM} the spatial width and τ_{FWHM} the width of the temporal envelope of the electric field. The average power $\overline{P}$ can then be calculated by spatial and temporal integration

$$\overline{P} = P_{\mathrm{p}} f_{\mathrm{rep}} = I_0 \sqrt{\frac{\pi^3}{2(\ln(2))^3}} \times \frac{f_{\mathrm{rep}} \sigma^2_{\mathrm{FWHM}} \tau_{\mathrm{FWHM}}}{4}, \tag{34}$$

where f_{rep} is the repetition rate of the laser and P_{p} is the pulse energy. In our measurements, the power was measured before an aperture used to optimize harmonic generation. The transmitted power through the iris can be estimated by integration of equation (33), resulting in

$$\overline{P}_{\mathrm{trans}} = \overline{P}\left(1 - \exp\left(-4\ln(2)\frac{D_0^2}{d^2_{\mathrm{FWHM}}}\right)\right), \tag{35}$$

where d_{FWHM} is the beam width before the iris and D_0 is the iris diameter. It follows

$$I_0 = 4P_{\mathrm{p}}\left(1 - \exp\left(-4\ln(2)\frac{D_0^2}{d^2_{\mathrm{FWHM}}}\right)\right) \times \sqrt{\frac{2(\ln(2))^3}{\pi^3}} \left(f_{\mathrm{rep}} \sigma^2_{\mathrm{FWHM}} \tau_{\mathrm{FWHM}}\right)^{-1}. \tag{36}$$

At a typical total generation pulse energy of 2 mJ, $\sigma_{\mathrm{FWHM}} = 80\,\mu$m, $\tau_{\mathrm{FWHM}} = 32$ fs and $D_0 = 7$ mm (see section II B) the resulting peak intensity is estimated, using equation (36), to be $3.5 \cdot 10^{14} \frac{\mathrm{W}}{\mathrm{cm}^2}$. The relationship between electric field and intensity allows us to calculate $E_0(D_0 = 7\,\mathrm{mm}) = \sqrt{2 I_0 c n \epsilon_0} = 5.1 \cdot 10^{10} \frac{\mathrm{V}}{\mathrm{m}} = 0.1\,\mathrm{a.u.}$. It has to be noted, that the iris diameter was only measured to about ±1mm. Since σ_{FWHM} is a function of D_0, where no analytic form is available, an error propagation calculation is difficult. However, if we apply the same kind of estimation to an iris diameter of 6 mm one obtains $E_0(D_0 = 6\,\mathrm{mm}) = 0.08\,\mathrm{a.u.}$ giving an indication of the uncertainty of the given value. As the spatial width of the focal spot was not measured, but a calculated value was taken instead, the stated number has to be considered to be an estimation of the upper bound. This is typically the case because the experimental spot size is underestimated as a consequence of the M^2 parameter of the laser, as well as due to propagation effects in the semi-infinite gas cell.

III. RESULTS

A. Photon Flux

This section describes the behavior of the photon flux as a function of the generation pressure and the input power. Our experimental and theoretical results are presented in figure 16. In the experiments, a strong dependence of the pressure on the obtained flux is observed. The obtained flux changes by an order of magnitude within a pressure range of 20 mbar. For all harmonics, a saturation of the flux starting around an input-pulse energy of 2 to 3 mJ is observed. The photon flux for the individual harmonics was found to be up to 10^6 photons per pulse when generating in argon. The photon flux was found to increase selectively for individual harmonics by using an aperture infront of the focusing optic.

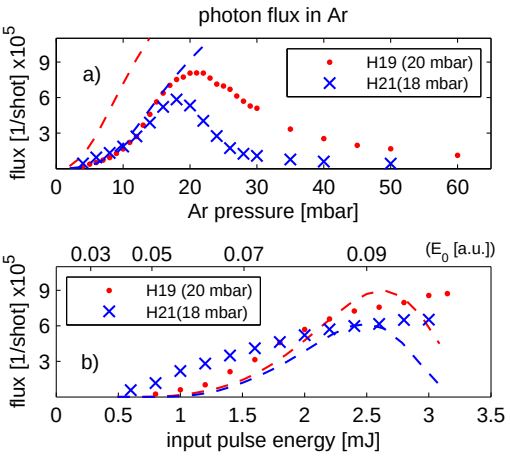

FIG. 16. Measured photon flux when generating in argon gas. a) as a function of the argon gas pressure in the high-pressure region (HP) and b) as a function of the pulse energy of the driving laser. The optimal generation pressure is found to be different for each harmonic order. A saturation of the photon flux for high energies was observed. All data points belonging to one harmonic order have been measured with the same iris diameter. The dashed curves represent calculations with the model presented in section II G for $z_{\mathrm{foc}} = 10$ mm and $E_0 = 0.09$ a.u.. The theory curves are scaled such as to fit the peak flux for H21 in the intensity scaling.

Using the model presented in section II G, the saturation of the flux as function of intensity is well reproduced. This effect is associated with phase matching due to plasma generation, therefore generation gases with a lower I_{p} than argon will saturate already at lower energies and vice versa. The relative peak flux of the harmonics as function of intensity is also well reproduced. The values for E_0 given in the figure are estimations since the spatially dependent intensity in the focal region cannot be stated accurately. The pressure dependence is well reproduced only for H21 and also there only for pressures lower than 20 mbar. This however is expected for several reasons. First, we implicitly assume that the spatial pressure distribution is independent of the pressure in the high pressure region. It is well known that there is a strong nonlinear dependence in this pressure range of the backing pressure on both the molecular or atomic flux through the aperture as well as on the angular distribution and intensity of the emerging gas jet[78,79]. This effect is observable in our experiments in the clear non-linear behavior of the pressure in the first differential pumping stage as function of the pressure in the high-pressure region (see Tab. II). This does not however, imply that the presented model is ill suited for high or low pressure regions. Second, we could only estimate the reference refractive index for H19 due to the presence of resonances. Third, the nonlinear refractive index is equally dependent on the gas density as the linear refractive index. The influence of nonlinear processes on the obtained photon flux will therefore be more significant for higher pressures.

Several general conclusions can be drawn from the model. First, we do not expect a significant difference in the obtained photon flux in the region of optimal flux for the semi-infinite gas cell as compared to a finite gas cell. This is because we see that the effective generation region is only few millimeters (see figure 15) which can be easily achieved with a finite gas cell. It has to be clarified that this statement is valid for the low-order harmonics in argon. When generating in other gases with lower absorption coefficients (see Tab. I), the effective maximal phase matching length becomes important. This leads to our second conclusion - for the generation with a short effective generation length, the spatial variation of pressure at the pinhole contributes significantly to the phase matching and hence to the total observed flux. For the optimal flux in the given range of pulse energies we found two distinct maxima for the focus position relative to the pinhole. The first position, lying inside the high pressure medium is however not accessible for focal field strengths higher than $E_0 = 0.07$ due to the significant ionization fraction leading to nonlinear effects not included in our model. Experimentally these two areas of favorable phase-matching could be observed however a detailed characterization was not performed. For the second position, the location of maximal flux is always such that the effective field strength at the generation region is in the order of 0.06 a.u. to 0.07 a.u.. This is not surprising since for higher field strengths the plasma contribution starts to dominate making phase matching impossible. Hence the third conclusion, for phase-matched generation in the high-flux region of our parameter space only a low cutoff can be achieved for the HHG.

The typical photon flux reported for this type of monochromators is on the order of 10^6 to 10^7 photons per shot depending on the specific experimental conditions.[7–10,12] It has to be acknowledged that the values we give here are on the lower edge of this range, particularly compared to Ref.[7] where a flux of 10^6 photons per shot is reported for a ten times lower pulse energy at otherwise similar experimental conditions. Further work

is necessary to establish the reason behind this discrepancy.

B. Pulse Duration

The XUV pulse duration of individual harmonic orders was measured through cross-correlation with an IR pulse as described in section II D. Due to a systematic deviation discussed below we neglected the XUV - IR pathway for H17 for the estimation of the XUV pulse duration. For all other channels the temporal widths of XUV + IR and XUV - IR sidebands were averaged and the standard deviation of the average was calculated. The absolute XUV pulse duration was then calculated using equation (5). Fig. 17 shows that the obtained pulse lengths generally decrease with increasing harmonic order.

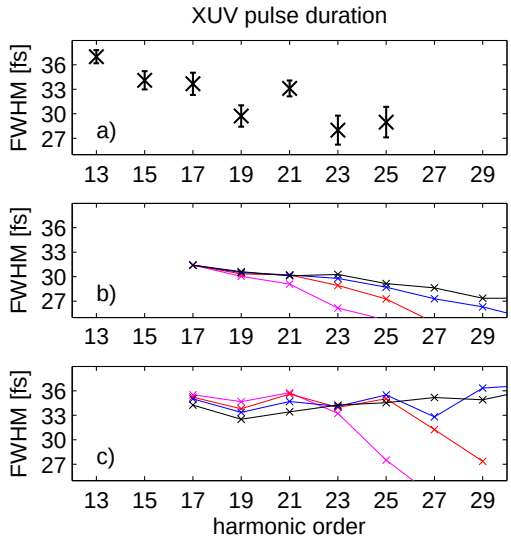

FIG. 17. Panel a) shows the measured pulse duration of the individual harmonic orders calculated according to equation (5). The error bars give the standard deviation calculated by error propagation from the standard deviation of the average of the two sidebands of 5 independent measurements for each harmonic order. Panel b) displays the calculated pulse duration taking into account only the temporal emission profile and neglecting the effect of the XUV far-field profile. A constant positive shift of 15.7, 14.7, 13.9, 13.3 fs has been applied to the curves for $E_0 = 0.05, 0.06, 0.07, 0.08$ a.u. respectively to match the measured FWHM of H17. Panel c) displays the calculated pulse duration using the presented SFA model taking into account the XUV far-field profile as well. The color code is the same as in figures 9 and 11.

The observation of a decreasing pulse duration with increasing harmonic order is consistent with equation (4) using the results from sections II E and II F. This result is thereby confirming the interplay between the harmonic order dependent illumination of the grating and the pulse duration inherent to the generation process of the XUV. Considering the temporal emission profile alone an intensity dependent constant offset has to be applied to achieve an agreement with the measurement. For the complete model absolute pulse durations as well as their trend as a function of the harmonic order agree reasonably well with the experiment. The best agreement is achieved for a maximal electric field strength between 0.05 a. u. and 0.06 a. u.. The agreement is surprising given the complete neglect of phase matching and the relatively crude approximations. One reason for this could be that the cross correlation experiments were always performed at comparably low pressures in the gas cell and at low laser intensities to suppress spectral and temporal broadening of the XUV. The stated values for the electric field strength are consistent with the estimated upper bound of the experimental field strength (see section II H).

As pointed out above the sideband corresponding to XUV + IR photoionization and the sideband corresponding to XUV - IR photoionization of harmonic 17, both showed a systematic deviation of their temporal widths (see Fig. 18). Harmonic 17 of 800 nm corresponds to a photon energy of 26.35 eV. A small blue-shift, typical for XUV generated by HHG[29,80], brings H17 into resonance with the $3s3p^6 4p$ state of Ar at 26.6 eV[71]. The XUV - IR pathway is then also resonant with the $3s3p^6 4s$ state at 25.17 eV[81]. The XUV + IR pathway can however not reach the $3s3p^6 4d$ state at 28.35 eV[81] because it lies outside the available bandwidth. The observed deviation in cross-correlation through the XUV - IR pathway may thus be a signature of the $3s^2 3p^6 \rightarrow 3s3p^6 4p \rightarrow 3s3p^6 4s$ double-resonant pathway. This interpretation is further supported by the facts that the H17 - IR sideband intensity is significantly enhanced compared to the H17 + IR sideband (not shown) and that the maximum of the former is shifted to negative delays (IR after XUV) as compared to the latter (see Fig. 18). A more detailed description of these dynamics will be given elsewhere.

C. Spectral Shape & Spectral Contrast

An important property for the application of this monochromator in time-resolved photoelectron spectroscopy is the spectral shape and the spectral contrast of the generated radiation. We found that for our generation parameters the FWHM spectral width of the XUV was on the order of 250 to 350 meV depending on day-to-day alignment. The spectral contrast was qualified by measuring residual transmission of neighboring harmonics. Figures 4 and 5 show that this measurement depends on the dimension of the selection slit as well as the harmonic order and the given spectral width of the harmonic. As described in section II C, a 300 μm slit was used for the experiments presented here. For this particular slit size the ratio between the photoelectron counts related to residual harmonics divided by the peak photoelectron counts of the selected harmonic was determined. This ratio was found to be better than 1/100 for

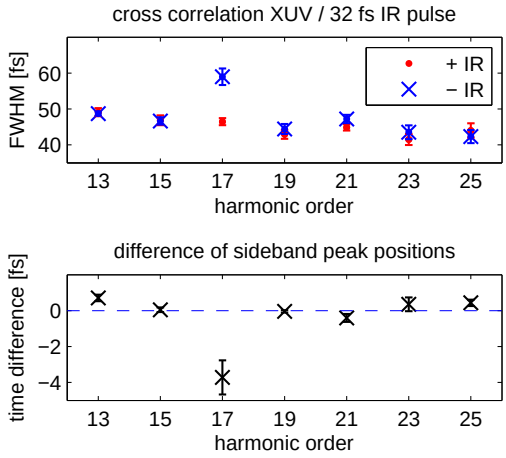

FIG. 18. Top: Width of the individual sidebands as a function of harmonic order. For harmonic 17 a systematic deviation was observed and is discussed in the text. The error bars given are the standard deviation of the average of 5 independent measurements. Bottom: Difference in the delay position of the XUV + IR and the XUV - IR sideband maxima. Negative delays correspond to the IR pulse reaching the interaction region after the XUV.

all harmonic orders between 13 and 25. Fig. 19 shows an exemplary data set for harmonic 15 on a logarithmic intensity scale.

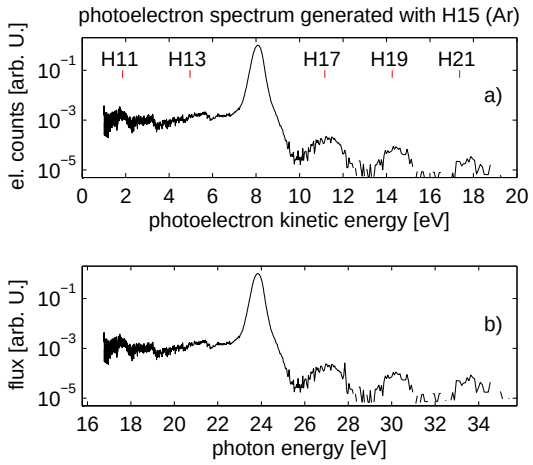

FIG. 19. a) Normalized and Jacobi corrected photoelectron spectrum of Ar ionized with H15 (23.25 eV). The peak at 8.1 eV corresponds to one-photon ionization from the ground state. b) The spectrum from a) corrected by the photoabsorption crossection taken from[46]. The different energetic width of the photoelectron peaks towards higher kinetic energies is a consequence of the decreasing resolution of the MBES.

IV. CONCLUSION

We have presented a pulsed femtosecond XUV light source based on a semi-infinite gas cell coupled to a conical-diffraction monochromator. We have characterized the XUV pulses obtained in terms of flux, pulse duration and spectral contrast. It was found that the flux strongly depends on the generation conditions and that the optimal parameters significantly depend on the harmonic order. This behavior was rationalized by phase-matching calculations and attributed to an interplay between several effects, the most dominant ones being the ionization induced phase contribution and the spatially dependent pressure. The typical flux achieved in this setup is on the order of 10^6 photons per shot and harmonic order, recalling that the measured number is a lower bound to the actual flux. The pulse duration decreases with increasing harmonic order. This effect was attributed to an interplay between the harmonic-order-dependent divergence of the XUV, leading to an order-dependent illumination of the grating, and the inherent pulse duration due to the generation process. The latter contribution scales approximately linearly with the pulse duration of the fundamental beam and therefore the XUV pulse duration will decrease correspondingly when working with shorter pulses. For XUV pulse durations below about 20 fs a second grating is necessary to compensate for the geometrical time spread[7,42]. We find the residual pulse energy of neighboring harmonic orders to be at least a factor of 100 smaller than the selected harmonic order, this contrast factor being higher for lower orders. The described characteristics of this instrument are promising for applications in time-resolved photoionization and photoelectron spectroscopies in the gas and condensed phases.

ACKNOWLEDGMENTS

The research leading to these results has received funding from the European Research Council under the European Union's Seventh Framework Programme (FP/2007-2013) / ERC Grant Agreement no. 307270-ATTOSCOPE and the National Centre of Competence in Research Molecular Ultrafast Science and Technology (NCCR-MUST), a research instrument of the Swiss National Science Foundation (SNSF). We thank Prof. P. Chen for his donation of the MBES used in this work. We also acknowledge helpful discussions with Prof. M. Ivanov and Prof. A. L'Huillier. Further we would like to thank U. Müller from the Swiss Federal Laboratories for Materials Science and Technology (EMPA) for providing the coatings of the toroidal mirrors. The authors would like to express their gratitude to the electronic and mechanical workshop of ETHZ/D-CHAB in particular to M. Kerellaj, A. Laso and A. Schneider.

[1] J. Berkowitz, *Photoabsorption, Photoionization, and Photoelectron Spectroscopy* (Elsevier Inc., 1979).

[2] K. Kimura, S. Katsumata, Y. Achiba, T. Yamazaki, and S. Iwata, *Handbook of HeI photoelectron spectra* (Japan Scientific Societies Press, Tokyo, 1981).

[3] U. Becker and D. A. Shirley, eds., *VUV and Soft X-Ray Photoionization* (Plenum Press, New York, 1996).

[4] P. Siffalovic, M. Drescher, M. Spieweck, T. Wiesenthal, Y. C. Lim, R. Weidner, A. Elizarov, and U. Heinzmann, Review of Scientific Instruments **72**, 30 (2001).

[5] L. Nugent-Glandorf, M. Scheer, D. A. Samuels, A. M. Mulhisen, E. R. Grant, X. Yang, V. M. Bierbaum, and S. R. Leone, Phys. Rev. Lett. **87**, 193002 (2001).

[6] J. Gaudin, S. Rehbein, P. Guttmann, S. Godé, G. Schneider, P. Wernet, and W. Eberhardt, Journal of Applied Physics **104**, 033112 (2008).

[7] L. Poletto, P. Villoresi, F. Frassetto, F. Calegari, F. Ferrari, M. Lucchini, G. Sansone, and M. Nisoli, Review of Scientific Instruments **80**, 123109 (2009).

[8] M. Ito, Y. Kataoka, T. Okamoto, M. Yamashita, and T. Sekikawa, Opt. Express **18**, 6071 (2010).

[9] P. Wernet, J. Gaudin, K. Godehusen, O. Schwarzkopf, and W. Eberhardt, Review of Scientific Instruments **82**, 063114 (2011).

[10] F. Frassetto, C. Cacho, C. A. Froud, I. E. Turcu, P. Villoresi, W. A. Bryan, E. Springate, and L. Poletto, Opt. Express **19**, 19169 (2011).

[11] S. Demmler, J. Rothhardt, S. Hädrich, M. Krebs, A. Hage, J. Limpert, and A. Tünnermann, Opt. Lett. **38**, 5051 (2013).

[12] B. Frietsch, R. Carley, K. Däbrich, C. Gahl, M. Teichmann, O. Schwarzkopf, P. Wernet, and M. Weinelt, Review of Scientific Instruments **84**, 075106 (2013).

[13] J. Metje, M. Borgwardt, A. Moguilevski, A. Kothe, N. Engel, M. Wilke, R. Al-Obaidi, D. Tolksdorf, A. Firsov, M. Brzhezinskaya, A. Erko, I. Y. Kiyan, and E. F. Aziz, Opt. Express **22**, 10747 (2014).

[14] T. Suzuki, Annual Review of Physical Chemistry **57**, 555 (2006).

[15] Y. Arasaki and K. Takatsuka, Chemical Physics **338**, 175 (2007).

[16] T. Horio, T. Fuji, Y.-I. Suzuki, and T. Suzuki, Journal of the American Chemical Society **131**, 10392 (2009), pMID: 19591468.

[17] Y. Arasaki, K. Takatsuka, K. Wang, and V. McKoy, The Journal of Chemical Physics **132**, 124307 (2010).

[18] C. Z. Bisgaard, O. J. Clarkin, G. Wu, A. M. D. Lee, O. Geßner, C. C. Hayden, and A. Stolow, Science **323**, 1464 (2009).

[19] M. Ferray, A. L'Huillier, X. F. Li, L. A. Lompre, G. Mainfray, and C. Manus, Journal of Physics B: Atomic, Molecular and Optical Physics **21**, L31 (1988).

[20] P. B. Corkum, Phys. Rev. Lett. **71**, 1994 (1993).

[21] M. Lewenstein, P. Balcou, M. Y. Ivanov, A. L'Huillier, and P. B. Corkum, Phys. Rev. A **49**, 2117 (1994).

[22] P. Salières, A. L'Huillier, and M. Lewenstein, Phys. Rev. Lett. **74**, 3776 (1995).

[23] C. Delfin, C. Altucci, F. D. Filippo, C. de Lisio, M. B. Gaarde, A. L'Huillier, L. Roos, and C.-G. Wahlström, Journal of Physics B: Atomic, Molecular and Optical Physics **32**, 5397 (1999).

[24] A. Rundquist, C. G. Durfee, Z. Chang, C. Herne, S. Backus, M. M. Murnane, and H. C. Kapteyn, Science **280**, 1412 (1998).

[25] A. Paul, R. A. Bartels, R. Tobey, H. Green, S. Weiman, I. P. Christov, M. M. Murnane, H. C. Kapteyn, and S. Backus, Nature **421**, 51 (2003).

[26] N. Papadogiannis, C. Kalpouzos, E. Goulielmakis, G. Nersisyan, D. Charalambidis, F. Augé, F. Weihe, and P. Balcou, Applied Physics B **73**, 687 (2001).

[27] J. Peatross, J. R. Miller, K. R. Smith, S. E. Rhynard, and B. W. Pratt, Journal of Modern Optics **51**, 2675 (2004).

[28] J. Sutherland, E. Christensen, N. Powers, S. Rhynard, J. Painter, and J. Peatross, Opt. Express **12**, 4430 (2004).

[29] D. S. Steingrube, T. Vockerodt, E. Schulz, U. Morgner, and M. Kovačev, Phys. Rev. A **80**, 043819 (2009).

[30] J.-P. Brichta, M. C. H. Wong, J. B. Bertrand, H.-C. Bandulet, D. M. Rayner, and V. R. Bhardwaj, Phys. Rev. A **79**, 033404 (2009).

[31] M. S. Hunter and P. Fowle, Journal of The Electrochemical Society **103**, 482 (1956).

[32] R.-P. Haelbich and C. Kunz, Optics Communications **17**, 287 (1976).

[33] A.-S. Morlens, R. López-Martens, O. Boyko, P. Zeitoun, P. Balcou, K. Varjú, E. Gustafsson, T. Remetter, A. L'Huillier, S. Kazamias, J. Gautier, F. Delmotte, and M.-F. Ravet, Opt. Lett. **31**, 1558 (2006).

[34] K. T. Kim, C. M. Kim, M.-G. Baik, G. Umesh, and C. H. Nam, Phys. Rev. A **69**, 051805 (2004).

[35] A. Wonisch, T. Westerwalbesloh, W. Hachmann, N. Kabachnik, U. Kleineberg, and U. Heinzmann, *Proceedings of the 7th International Symposium on Atomically Controlled Surfaces, Interfaces and Nanostructures*, Thin Solid Films **464-465**, 473 (2004).

[36] J. Kirz, J. Opt. Soc. Am. **64**, 301 (1974).

[37] B. Niemann, D. Rudolph, and G. Schmahl, Optics Communications **12**, 160 (1974).

[38] U. Vogt, M. Wieland, T. Wilhein, M. Beck, and H. Stiel, Review of Scientific Instruments **72**, 53 (2001).

[39] M. Neviere, D. Maystre, and W. R. Hunter, J. Opt. Soc. Am. **68**, 1106 (1978).

[40] W. Cash, Appl. Opt. **21**, 710 (1982).

[41] W. Werner and H. Visser, Appl. Opt. **20**, 487 (1981).

[42] M. Pascolini, S. Bonora, A. Giglia, N. Mahne, S. Nannarone, and L. Poletto, Appl. Opt. **45**, 3253 (2006).

[43] W. Cash and R. Kohnert, Appl. Opt. **21**, 17 (1982).

[44] J. F. Seely, L. I. Goray, B. Kjornrattanawanich, J. M. Laming, G. E. Holland, K. A. Flanagan, R. K. Heilmann, C.-H. Chang, M. L. Schattenburg, and A. P. Rasmussen, Appl. Opt. **45**, 1680 (2006).

[45] D. S. Steingrube, E. Schulz, T. Binhammer, M. B. Gaarde, A. Couairon, U. Morgner, and M. Kovacev, New Journal of Physics **13**, 043022 (2011).

[46] J. A. Samson, *The Measurement of the Photoionization Cross Sections of the Atomic Gases*, Vol. Volume 2 (Academic Press, 1966) pp. 177–261.

[47] Z. Chang, *Fundamentals of Attosecond Optics* (CRC Press, 2011).

[48] W. Werner, Appl. Opt. **16**, 2078 (1977).

[49] P. Salières, T. Ditmire, M. D. Perry, A. L'Huillier, and M. Lewenstein, Journal of Physics B: Atomic, Molecular and Optical Physics **29**, 4771 (1996).

[50] B. Henke, E. Gullikson, and J. Davis, Atomic Data and Nuclear Data Tables **54**, 181 (1993).

[51] M. Huppert, I. Jordan, and H. J. Wörner, Review of Scientific Instruments **86**, 123106 (2015).

[52] H.-J. Hagemann, W. Gudat, and C. Kunz, J. Opt. Soc. Am. **65**, 742 (1975).

[53] P. Kruit and F. H. Read, Journal of Physics E: Scientific Instruments **16**, 313 (1983).

[54] M. Galanti, R. Gott, and J. F. Renaud, Review of Scientific Instruments **42**, 1818 (1971).

[55] T. E. Glover, R. W. Schoenlein, A. H. Chin, and C. V. Shank, Phys. Rev. Lett. **76**, 2468 (1996).

[56] L. Poletto, P. Villoresi, E. Benedetti, F. Ferrari, S. Stagira, G. Sansone, and M. Nisoli, J. Opt. Soc. Am. B **25**, B44 (2008).

[57] V. S. Yakovlev, M. Ivanov, and F. Krausz, Opt. Express **15**, 15351 (2007).

[58] M. Y. Ivanov, T. Brabec, and N. Burnett, Phys. Rev. A **54**, 742 (1996).

[59] G. L. Yudin and M. Y. Ivanov, Phys. Rev. A **64**, 013409 (2001).

[60] H. J. Wörner, H. Niikura, J. B. Bertrand, P. B. Corkum, and D. M. Villeneuve, Phys. Rev. Lett. **102**, 103901 (2009).

[61] L. Keldysh, Sov. Phys. JETP **20**, 1307 (1965).

[62] A. L'Huillier, K. J. Schafer, and K. C. Kulander, Journal of Physics B: Atomic, Molecular and Optical Physics **24**, 3315 (1991).

[63] P. Antoine, A. L'Huillier, M. Lewenstein, P. Salières, and B. Carré, Phys. Rev. A **53**, 1725 (1996).

[64] Saleh and Teich, *Fundamentals of photonics* (Wiley-Interscience, 1991).
[65] J. D. Jackson, *Classical electrodynamics* (Wiley, 1999).
[66] M. Lewenstein, P. Salières, and A. L'Huillier, Phys. Rev. A **52**, 4747 (1995).
[67] E. Constant, D. Garzella, P. Breger, E. Mével, C. Dorrer, C. Le Blanc, F. Salin, and P. Agostini, Phys. Rev. Lett. **82**, 1668 (1999).
[68] A. Lago, G. Hilber, and R. Wallenstein, Phys. Rev. A **36**, 3827 (1987).
[69] G. Liggett and J. S. Levinger, J. Opt. Soc. Am. **58**, 109 (1968).
[70] F. W. King, J. Opt. Soc. Am. B **19**, 2427 (2002).
[71] S. L. Sorensen, T. Åberg, J. Tulkki, E. Rachlew-Källne, G. Sundström, and M. Kirm, Phys. Rev. A **50**, 1218 (1994).
[72] M. Bellini, C. Corsi, and M. C. Gambino, Phys. Rev. A **64**, 023411 (2001).
[73] A. Lytle, *Phase Matching and Coherence of High-Order Harmonic Generation in Hollow Waveguides*, Ph.D. thesis, Graduate School of the University of Colorado (2008).
[74] A. Bideau-Mehu, Y. Guern, R. Abjean, and A. Johannin-Gilles, Journal of Quantitative Spectroscopy and Radiative Transfer **25**, 395 (1981).
[75] M. Weber, *Handbook of Optical Materials* (CRC Press, 2002).
[76] P. D. Maker, R. W. Terhune, M. Nisenoff, and C. M. Savage, Phys. Rev. Lett. **8**, 21 (1962).
[77] S. Kazamias, D. Douillet, C. Valentin, F. Weihe, F. Augé, T. Lefrou, G. Grillon, S. Sebban, and P. Balcou, Phys. Rev. A **68**, 033819 (2003).
[78] J. M. Guevremont, S. Sheldon, and F. Zaera, Review of Scientific Instruments **71**, 3869 (2000).
[79] F. Rugamas, D. Roundy, G. Mikaelian, G. Vitug, M. Rudner, J. Shih, D. Smith, J. Segura, and M. A. Khakoo, Measurement Science and Technology **11**, 1750 (2000).
[80] C. Kan, C. E. Capjack, R. Rankin, and N. H. Burnett, Phys. Rev. A **52**, R4336 (1995).
[81] R. J. Tweed, F. Gelebart, and J. Peresse, Journal of Physics B: Atomic and Molecular Physics **9**, 2643 (1976).